Magnetotransport and electronic structure of the antiferromagnetic semimetal YbAs

W. Xie,[1] Y. Wu,[1] F. Du,[1] A. Wang,[1] H. Su,[1] Y. Chen,[1] Z. Y. Nie,[1] S.-K. Mo,[2] M. Smidman,[1,*] C. Cao,[3] Y. Liu,[1,4,†] T. Takabatake,[1,5] and H. Q. Yuan[1,4,‡]

[1]*Center for Correlated Matter and Department of Physics, Zhejiang University, Hangzhou 310058, China*
[2]*Advanced Light Source, E. O. Lawrence Berkeley National Lab, Berkeley, California 94720, USA*
[3]*Department of Physics, Hangzhou Normal University, Hangzhou 310036, China*
[4]*Collaborative Innovation Center of Advanced Microstructures, Nanjing University, Nanjing 210093, China*
[5]*Department of Quantum Matter, AdSM, Hiroshima University, Higashi-Hiroshima 739-8530, Japan*

(Received 26 June 2019; revised manuscript received 3 February 2020; accepted 4 February 2020; published 19 February 2020)

A number of rare-earth monopnictides have topologically nontrivial band structures together with magnetism and strong electronic correlations. In order to examine whether the antiferromagnetic (AFM) semimetal YbAs ($T_N = 0.5$ K) exhibits such a scenario, we have grown high-quality single crystals using a flux method, and characterized the magnetic properties and electronic structure using specific heat, magnetotransport, and angle-resolved photoemission spectroscopy (ARPES) measurements, together with density functional theory (DFT) calculations. Both ARPES and DFT calculations find no evidence for band inversions in YbAs, indicating a topologically trivial electronic structure. From low-temperature magnetotransport measurements, we map the field-temperature phase diagram, where we find the presence of a field stabilized phase distinct from the AFM phase at low temperatures. An extremely large magnetoresistance (XMR) for both YbAs and the nonmagnetic counterpart LuAs is also observed, which can consistently be accounted for by the presence of electron-hole compensation. Moreover, an angle-dependent study of the Shubnikov–de Haas effect oscillations reveals very similar Fermi surfaces between YbAs and LuAs, with light effective masses down to at least 0.5 K, indicating that the Yb-4f electrons are well localized, and do not contribute to the Fermi surface. However, the influence of the localized Yb-4f electrons on the magnetotransport of YbAs can be discerned from the distinct temperature dependence of the XMR compared to that of LuAs, which we attribute to the influence of short-ranged spin correlations that appear well above T_N.

DOI: 10.1103/PhysRevB.101.085132

I. INTRODUCTION

Searching for correlated and magnetic materials with topologically nontrivial electronic structures has recently led to the discovery of novel topological phases, such as topological Kondo insulators [1,2], magnetic topological insulators [3–6], magnetic Weyl semimetals [7–10], and Weyl-Kondo semimetals [11,12]. The *LnX* series crystallizing in the cubic NaCl-type structure [13] (*Ln* = rare earth and *X* = As, Sb, or Bi) is a large family of semimetals where topologically nontrivial band structures have been found to exist with electronic correlations and magnetism [14–32]. For example, evidence was found that CeSb hosts Weyl fermions in the field-induced ferromagnetic state [14], while NdSb was reported to be a Dirac semimetal with antiferromagnetic (AFM) order [25–27]. Meanwhile in SmSb, the analysis of the Shubnikov–de Haas (SdH) oscillations indicates a topologically nontrivial band structure [29]. Topological electronic structures were detected using angle-resolved photoemission spectroscopy (ARPES) for several rare-earth monobismuthides (Ce, Pr, Sm, Gd)Bi, showing tunable bulk band inversions and corresponding surface states [30], where the ARPES results agree well with density functional theory (DFT) calculations assuming the 4f electrons to be well localized [32].

Yb-monopnictides are also promising candidates for studying topological systems with electronic correlations and magnetism, but the topology of the electronic structures has not been reported. In this work we focus on one example YbAs, which is an antiferromagnet with a Néel temperature $T_N = 0.5$ K [33]. Heavy fermion behavior was reported from several results, including a greatly reduced entropy of $0.2R\ln 2$ released at T_N together with a reduced ordered moment of 0.85 μ_B/Yb [33–36], and a huge value of the nuclear relaxation rate $1/(T_1T)$ below 0.2 K [37]. On the other hand, the resistivity $\rho(T)$ shows metallic behavior, without a logarithmic temperature dependence or Kondo coherence peak [38], and the carrier concentration $n \sim 10^{20}$ cm^{-3} is only about 1% of the magnetic Yb ions, which is far less than that required for full Kondo screening [38]. A de Haas–van Alphen (dHvA) effect study revealed the presence of three ellipsoidal electron pockets and one spherical hole pocket, where the charge carriers all have rather small effective masses [39].

Various scenarios have been proposed to account for the seemingly contradictory experimental results [36,38,40–44], among which the *p*-*f* mixing model has been widely discussed [38–40,45]. In this scenario, the hole states become

*msmidman@zju.edu.cn
†yangliuphys@zju.edu.cn
‡hqyuan@zju.edu.cn

heavy, but the electrons remain light and mobile, and therefore the metallic behavior of $\rho(T)$ is explained by electrons dominating the transport properties, while the additional hole pockets not detected in previous dHvA studies are expected to have large effective charge carrier masses, accounting for the greatly enhanced Sommerfeld coefficient [39,45]. On the other hand, inelastic neutron scattering (INS) measurements reveal the development of short-range spin correlations below around 20 K [46,47], which may also explain the reduced magnetic entropy at T_N, which is gradually released up to 20 K where the spin correlations disappear. As a result, the reduced ordered moment was proposed to arise due to the coexistence of short-range correlations with long-range magnetic order [47].

In this work we address several issues by studying high-quality single crystals of YbAs. We first characterize the low-temperature magnetism by determining the response of the magnetic transition to applied magnetic fields, and we construct a temperature-field phase diagram. Moreover, to gain insight into the effect of correlations as well as the topology of the band structure, the Fermi surfaces and carrier effective masses were investigated via angle-dependent SdH oscillations, ARPES measurements, and DFT calculations. SdH oscillations reveal five Fermi surfaces pockets, one more than previous studies [39], and an analysis of the temperature dependence of the SdH amplitudes above T_N shows that the charge carriers of all pockets have light effective masses. Meanwhile, no evidence for a Kondo resonance was found from ARPES measurements down to 10 K, and the results are in good agreement with DFT calculations assuming well localized $4f$ electrons. Furthermore, these demonstrate the absence of band inversions in the electronic structure, and therefore a trivial band topology. On the other hand, an extremely large magnetoresistance is observed at low temperatures, which from the Kohler's rule scaling analysis and Hall measurements, can be ascribed to electron-hole compensation and large mobilities. Additional features are observed in the low temperature XMR of YbAs not present in the data of LuAs, which are likely due to the influence of short-ranged spin correlations on the magnetotransport.

II. EXPERIMENTAL DETAILS

Single crystals of YbAs and LuAs were prepared using eutectic Pd-As binary phases as a flux, in contrast to previous studies where samples were grown using the Bridgman method [48]. Yb (or Lu) powder, Pd powder, and prereacted $PdAs_2$ were placed in an alumina crucible in the molar ratio 1:2:2. The crucible was sealed in an evacuated quartz tube. The mixture was slowly heated to 1000 °C in a muffle furnace and held there for one day. The furnace was then slowly cooled to 800 °C at a rate of about 1.8 °C/h, before the quartz tube was centrifuged to separate the crystals from the flux. Single crystals with a typical size of about $1 \times 1 \times 1$ mm^3 were obtained, as shown in the inset of Fig. 1(a).

The crystal structure and orientation were confirmed using x-ray diffraction (XRD) on a cleaved crystal using a PANalytical X'Pert MRD powder diffractometer with Cu $K_{\alpha 1}$ radiation monochromated by graphite. The chemical composition was determined by energy-dispersive x-ray spectroscopy using a Hitachi SU-8010 field emission scanning electron microscope. The resistivity and angle-dependent magnetotransport were measured using a Quantum Design Physical Property Measurement System (PPMS) with a sample rotation option.

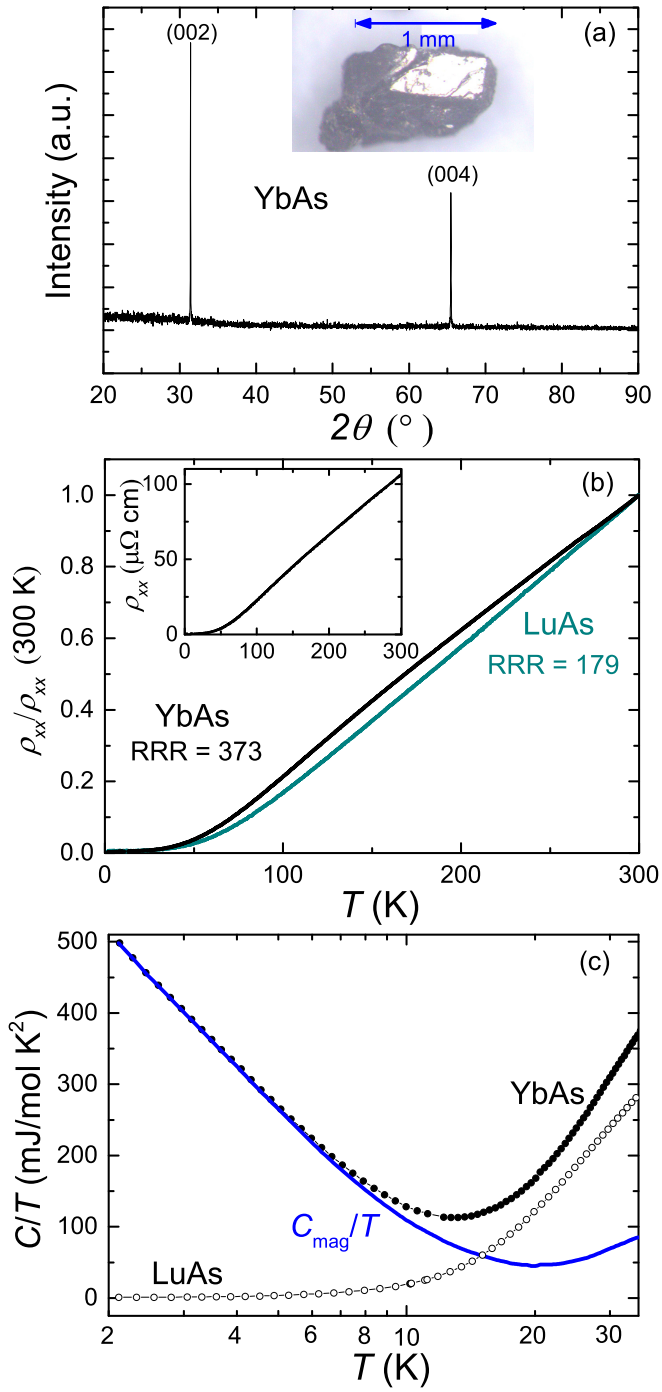

FIG. 1. (a) XRD pattern on an YbAs single crystal surface with the (001) plane. The inset shows a piece of single crystal with typical dimensions labeled. (b) Normalized temperature dependent resistivity $\rho_{xx}(T)$ for YbAs and LuAs in zero applied field. The inset of (b) displays the absolute value of $\rho_{xx}(T)$ of YbAs, where there is a small residual resistivity of 0.27 $\mu\Omega$ cm at 1.9 K. (c) Low-temperature heat capacity as C/T of YbAs and LuAs. The blue solid line displays the magnetic contribution to the heat capacity of YbAs.

Four Pt wires were attached to the sample using silver paste. The specific heat was also measured using a PPMS. The low-temperature MR between 0.275 and 10 K was measured using a ^{3}He system in fields up to 15 T. The Hall measurements were performed using a PPMS, utilizing a four-wire method on a piece of single crystal with the applied field perpendicular to the (111) plane and the current direction within the plane, where the transverse resistivity contribution was subtracted.

High-resolution ARPES measurements were carried out on the beamline 10.0.1 at the Advanced Light Source (ALS), Lawrence Berkeley National Laboratory (USA). The typical energy and angular resolution were about 15 meV and 0.2°, respectively. A photon energy range from 30 to 200 eV was used during the measurements. Single crystals of YbAs were cleaved *in situ* at around 20 K and measured at the same temperature. Temperature-dependent scans were performed from 13 up to 80 K, but no obvious temperature dependence was found in the ARPES spectra. All measurements were performed in an ultrahigh vacuum with a base pressure lower than 1×10^{-10} Torr.

Density functional theory (DFT) calculations were performed using the Vienna *ab initio* simulation package (VASP). A plane-wave basis up to 380 eV and $12 \times 12 \times 12$ Γ-centered K mesh were used to make sure the total energy converges to 1 meV per unit cell. The modified Becke-Johnson (mBJ) potentials were used with the effect of spin-orbit coupling (SOC) considered. The f electrons are treated as core states in all the calculations, which gives good agreement with experimental results.

III. RESULTS AND DISCUSSION

A. Sample characterization

Figure 1(a) shows an XRD pattern of a cleaved single crystal, in which the diffraction peak positions correspond to the (00l) plane of YbAs, indicating the correct phase of our crystals with the [001] direction perpendicular to the cleaved face. Figure 1(b) shows the normalized temperature dependence of the resistivity $\rho_{xx}(T)/\rho_{xx}(300\ \mathrm{K})$ from 300 to 1.9 K for YbAs and LuAs. Both display metallic behavior, and at elevated temperatures there is only a slight enhancement of the YbAs data over that of LuAs. The absolute resistivity of YbAs is shown in the inset, where the residual resistivity at 1.9 K is about 0.27 $\mu\Omega$ cm. For YbAs, the residual resistivity ratio RRR [$= \rho_{xx}(300\ \mathrm{K})/\rho_{xx}(1.9\ \mathrm{K})$] of 373 is more than one order of magnitude higher than previous studies [48]. The RRR of LuAs is about 179, which is also higher than that reported for polycrystalline samples [49]. The specific heat as C/T of LuAs monotonically decreases with temperature, and from fitting the low temperature data using $C/T = \gamma_n + \beta T^2$, a Sommerfeld coefficient of $\gamma_n = 0.15$ mJ/mol K^2 and $\beta = 0.14$ mJ/(mol K)^4 are obtained, where the latter corresponds to a Debye temperature of 302 K. In contrast, the C/T data of YbAs reaches a minimum at about 15 K, below which the data continue to increase with decreasing temperature. The magnetic contribution to the specific heat C_{mag}/T [Fig. 1(c)], obtained by subtracting the C/T of LuAs from that of YbAs, upturns below 20 K with a more rapid increase below about 8 K. This points to a significant low temperature contribution arising due to the presence of the Yb-4f electrons.

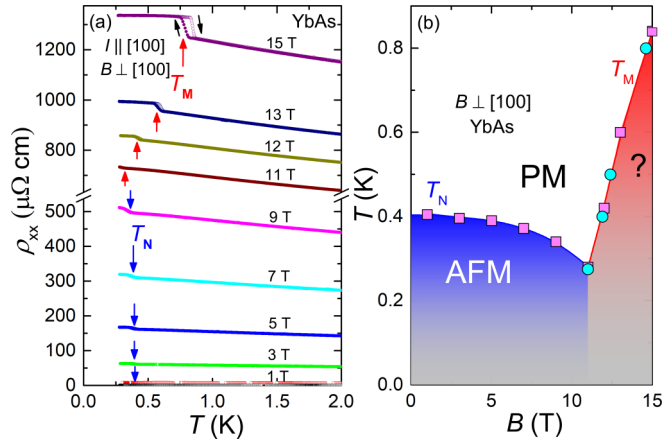

FIG. 2. (a) Temperature dependence of the resistivity (ρ_{xx}) of YbAs below 2 K measured in applied magnetic fields up to 15 T. The blue and red vertical arrows denote the transitions at T_N and T_M, respectively. (b) Temperature-field phase diagram of YbAs constructed from $\rho_{xx}(T)$ and $\rho_{xx}(B)$. The labels PM and AFM correspond to the paramagnetic phase and antiferromagnetic phase, respectively, while the nature of the phase below T_M is not yet determined.

B. *B*-*T* phase diagram

From low-temperature resistivity measurements in applied transverse fields, we determined the field dependence of T_N. Although $\rho_{xx}(T, 0)$ shows no detectable anomaly at $T_N = 0.5$ K [inset of Fig. 3(a)], clear jumps can be resolved in the in-field data. As shown in Fig. 2(a), T_N decreases with applied field up to 9 T, while above 11 T, a more pronounced jump appears in ρ_{xx} (denoted as T_M), which moves to higher temperature with increasing field. The solid black arrows in Fig. 2(a) denote the cooling and warming processes of the resistivity measurements. While a negligibly small thermal loop is found at T_N, above 11 T a sizable loop occurs at T_M, which becomes larger with increasing field. Note that the magnitude of the anomaly at the transition increases with field for both T_N and T_M. Based on $\rho_{xx}(T)$ and $\rho_{xx}(B)$, the B-T phase diagram of YbAs was constructed, as shown in Fig. 2(b).

A plausible explanation for the first order transition at T_M, which becomes increasingly stable with increasing magnetic field, is that this corresponds to the onset of quadrupolar ordering. This is supported by previous reports of a strong quadrupolar interaction in YbAs [50,51], where the quadrupolar moments could originate from the mixture of the CEF ground state Γ_6 and the first excited CEF state Γ_8 under applied magnetic fields. Other examples of field-induced quadrupolar ordering in rare earth compounds include $Dy_3Ru_4Al_{12}$ [52] and $HoFe_2Al_{10}$ [53]. However, this proposal is to be confirmed by further studies, such as ultrasound measurements.

C. MR and Hall resistivity

In the main panel of Fig. 3, $\rho_{xx}(T)$ under different applied magnetic fields is displayed for YbAs and LuAs down to 1.9 K. The field direction is perpendicular to the crystallographic plane and current direction, with $I \parallel [100]$ and $B \perp [100]$. As shown in the insets of Fig. 3, $\rho_{xx}(T, 0)$ flattens

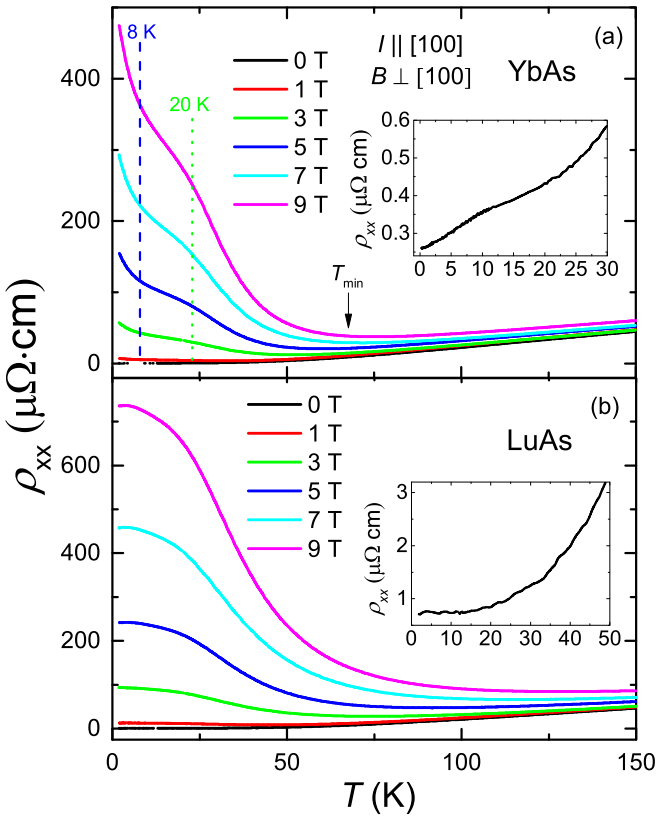

FIG. 3. Temperature dependence of the resistivity ρ_{xx} under various applied magnetic fields down to 1.9 K for (a) YbAs and (b) LuAs, with $B \perp I \| [100]$. Two characteristic temperatures are marked for YbAs. The insets of (a) and (b) show the low-temperature part of the zero field resistivity of YbAs and LuAs down to 0.275 K, respectively.

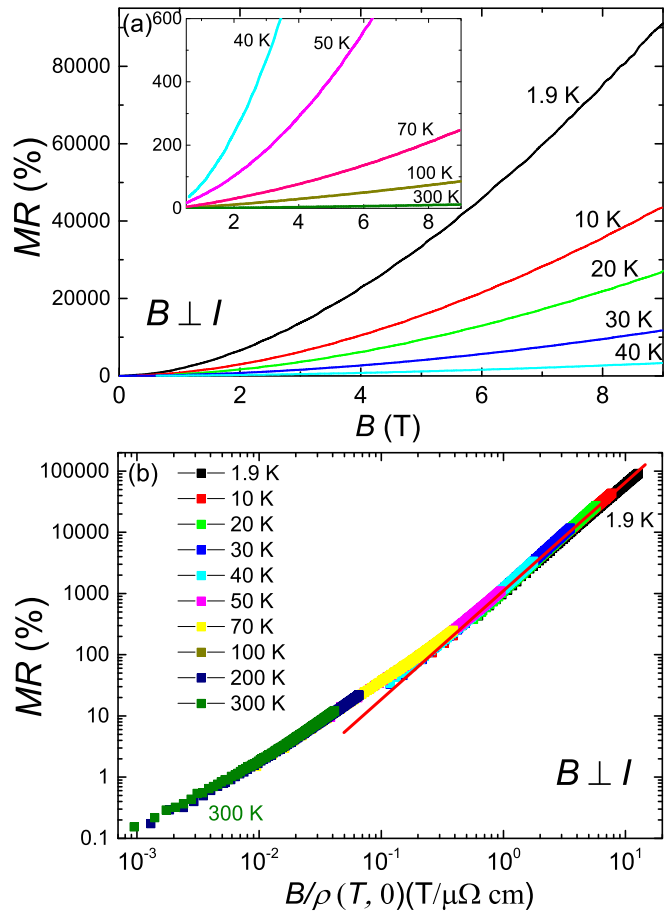

FIG. 4. (a) Transverse magnetoresistance of YbAs, measured at different temperatures from 300 to 1.9 K in fields up to 9 T. (b) Kohler's rule scaling of the magnetoresistance as a function of $B/\rho(T, 0)$.

below 10 K for LuAs, while $\rho_{xx}(T, 0)$ of YbAs has a change of slope at about 20 K, and decreases at a greater rate below 8 K, close to the temperature below which C_{mag}/T [Fig. 1(c)] begins to increase more rapidly. The temperature dependent resistivity $\rho_{xx}(T, B)$ of both YbAs and LuAs in a field starts to upturn below a temperature denoted as T_{min}, which increases with the applied field. For LuAs, a resistivity plateau develops below about 10 K, which is similar to other nonmagnetic XMR materials such as LaX [15,16,18]. However, the in-field resistivity of YbAs keeps rising down to 1.9 K, and there is a clear change of slope at 20 K, together with a more rapid increase below around 8 K. As shown in Fig. 2(a), the in-field $\rho_{xx}(T)$ continues to increase slightly at low temperatures, upon crossing the transitions at T_N or T_M. Here we note that INS measurements show that anomalous short-range antiferromagnetic spin correlations appear below 20 K, and the INS peak intensity increases more strongly with decreasing temperature below about 8 K [46,47]. These two temperatures correspond well to the anomalies observed in both the zero-field and in-field resistivity. The more rapid decreases in $\rho_{xx}(T, 0)$ upon lowering the temperature below 20 and 8 K (compared to that of LuAs) may be due to the reduction of spin-disorder scattering resulting from the development of short-range spin correlations, which are enhanced below 8 K. This behavior in the low temperature $\rho_{xx}(T, 0)$ can give rise to the features observed in the in-field $\rho_{xx}(T, B)$ of YbAs across the same temperature range, as shown below.

To gain more insights into the observed XMR, the MR(= $100\% \times [\rho_{xx}(T, B) - \rho_{xx}(T, 0)]/\rho_{xx}(T, 0)$) of YbAs was analyzed to look for the presence of Kohler's rule scaling, as performed for other nonmagnetic XMR materials [15,18,54]. Figure 4(a) displays the isothermal MR measured at various temperatures between 300 and 1.9 K, which is plotted as a function of $B/\rho(T, 0)$ in Fig. 4(b). It is apparent that the data at different temperatures fall onto a single line, showing that Kohler's rule is valid in YbAs [55]. Similar to WTe_2, this excludes the scenario of a metal-insulator transition being the origin of the field-induced resistivity upturn [54]. For WTe_2, the overall resistivity upturn behavior can be explained by Kohler's rule scaling,

$$MR = \alpha[B/\rho(T, 0)]^m, \quad (1)$$

with $m \simeq 2$, which can be derived from a two-band model with electron-hole compensation [54]. For YbAs as shown in Fig. 4(b), when the data are plotted on a double logarithmic scale, there is an apparent change in the slope at around 50–70 K, while below 50 K the data scale well linearly, with a fitted value of $m = 1.75$. Changes of the carrier concentration and/or mobility in the temperature range of 50–70 K may

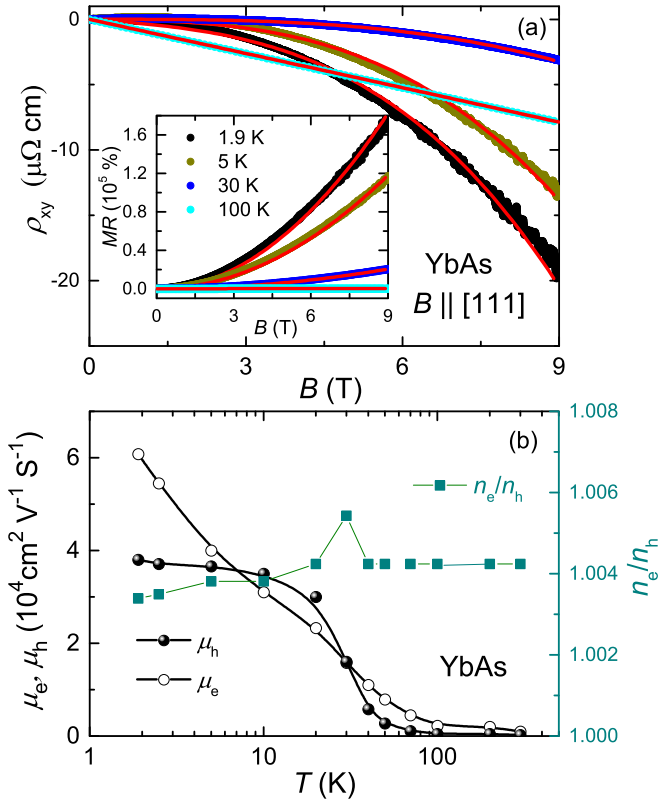

FIG. 5. (a) Field dependence of the Hall resistivity $\rho_{xy}(B)$ of YbAs, up to 9 T at 1.9, 5, 30, and 100 K. The inset shows the field dependent MR at the corresponding temperatures. The red solid lines in both the main panel and the inset show the results from fitting with a two-band model described in the text. (b) The temperature dependence of n_e/n_h, as well as the mobility of both electron and hole carriers, obtained from fitting both the MR and Hall resistivity with a two-band model.

account for this change of slope [18,54]. The presence of Kohler's scaling shows that $\rho(T, B)$ is solely determined by $\rho(T, 0)$. This suggests that in YbAs the unsaturated temperature dependence of the in-field resistivity is a reflection of the continuous decrease of $\rho(T, 0)$ [inset of Fig. 3(a)], which is most likely due to the reduced spin-disorder scattering arising from the development of antiferromagnetic correlations in the corresponding temperature range.

The Hall resistivity $\rho_{xy}(T, B)$ was also measured, so as to probe the temperature dependence of carrier concentration or mobility. As displayed in Fig. 5(a), $\rho_{xy}(B)$ for $T > 50$ K exhibits a nearly linear field dependence, while it is nonlinear below 50 K.

For a two-band model [18,55], $\rho_{xy}(B)$ and the MR can be expressed as

$$\rho_{xy} = \frac{B}{e}\frac{\left(n_h\mu_h^2 - n_e\mu_e^2\right) + (n_h - n_e)(\mu_e\mu_h)^2B^2}{(n_h\mu_h + n_e\mu_e)^2 + (n_h - n_e)^2(\mu_e\mu_h)^2B^2}, \quad (2)$$

$$MR = \frac{n_e\mu_e n_h\mu_h(\mu_e + \mu_h)^2B^2}{(n_h\mu_h + n_e\mu_e)^2 + (n_h - n_e)^2(\mu_e\mu_h)^2B^2}. \quad (3)$$

where n_e and n_h are the carrier concentrations of electrons and holes, respectively, while μ_e and μ_h are the respective mobilities.

Both $\rho_{xy}(B)$ and the MR were simultaneously fitted using Eqs. (2) and (3), and the fitted curves at several temperatures are displayed in Fig. 5(a). Due to the large number of parameters, n_e was fixed to the value of 4.74×10^{20} cm^{-3} from the analysis of the SdH oscillations (see below). Here we note that while this model is relatively insensitive to the absolute values of n_e and n_h, the ratio n_e/n_h is well constrained. In Fig. 5(b), the temperature dependence of the fitted values of n_e/n_h, μ_e, and μ_h are displayed. It can be seen that both μ_e and μ_h show a significant increase upon cooling below about 70 K, which may explain the change of exponent in the Kohler's rule scaling. The large values of the mobilities, reaching 4–6 m^2/(V s) at 1.9 K, can also account for the large magnetoresistance at low temperatures. Note that these mobilities are quite different from previous results [56], where only the electron mobility displays a weak increase below about 80 K, and the values are an order of magnitude lower. We ascribe this difference to the higher quality of our single crystals, manifested in the much larger RRR value. The fitted electron- and hole-carrier densities are nearly compensated over the whole temperature range ($n_e/n_h \approx 1$), in agreement with previous reports [56]. Therefore the combination of the validity of Kohler's rule scaling and the analysis of the magnetotransport with a two-band model indicates that electron-hole compensation is the main mechanism for the observed XMR [15,18,54]. In particular, the large mobilities at low temperatures for both electrons and holes could help realize the XMR in YbAs [15], but is different to that expected for the p-f mixing model, which predicts that the mobility of the electrons is much larger than the holes [38,56].

D. Fermi surfaces

1. SdH oscillations

To gain more insight into the electronic structure and to examine the band topology of YbAs and LuAs, we studied the Fermi surfaces using angle-dependent SdH oscillations measurements. Clear SdH oscillations are observed in the MR of YbAs at temperatures up to ~10 K in fields above 6 T, and to further examine the low temperature behavior, MR measurements in fields up to 15 T and down to 0.275 K were performed, and the results are displayed in the main panel of Fig. 6(a). Meanwhile the data for LuAs down to 1.9 K and up to 9 T are shown in Fig. 6(b). Angle-dependent ρ_{xx} measurements were also performed for both YbAs [inset of Fig. 6(a)] and LuAs, for different angles θ between the applied field and the [001] direction, as illustrated in the inset of Fig. 6(b). After subtracting the background, the SdH oscillations were analyzed via fast Fourier transforms (FFT) for various values of θ, and the results are shown in Figs. 6(c) and 6(d). For both compounds, we find the presence of five principal frequencies (α, α', α'', β, and γ) and some harmonic frequencies, indicating multiple Fermi surface pockets. From comparing the FFT results between YbAs and LuAs at $\theta = 0°$, it can be seen that the frequencies of the α and γ pockets (F_α and F_γ) are very close, while the frequency of β pockets (F_β) of LuAs is slightly larger than that of YbAs and $F_{\alpha''}$ is slightly smaller. Note that α'' coincides with α' at $\theta = 0°$, while they are separated at $\theta = 45°$ and $\theta = 60°$ [Fig. 6(d)]. The FFT spectra of YbAs at 0.275 K are identical to those at

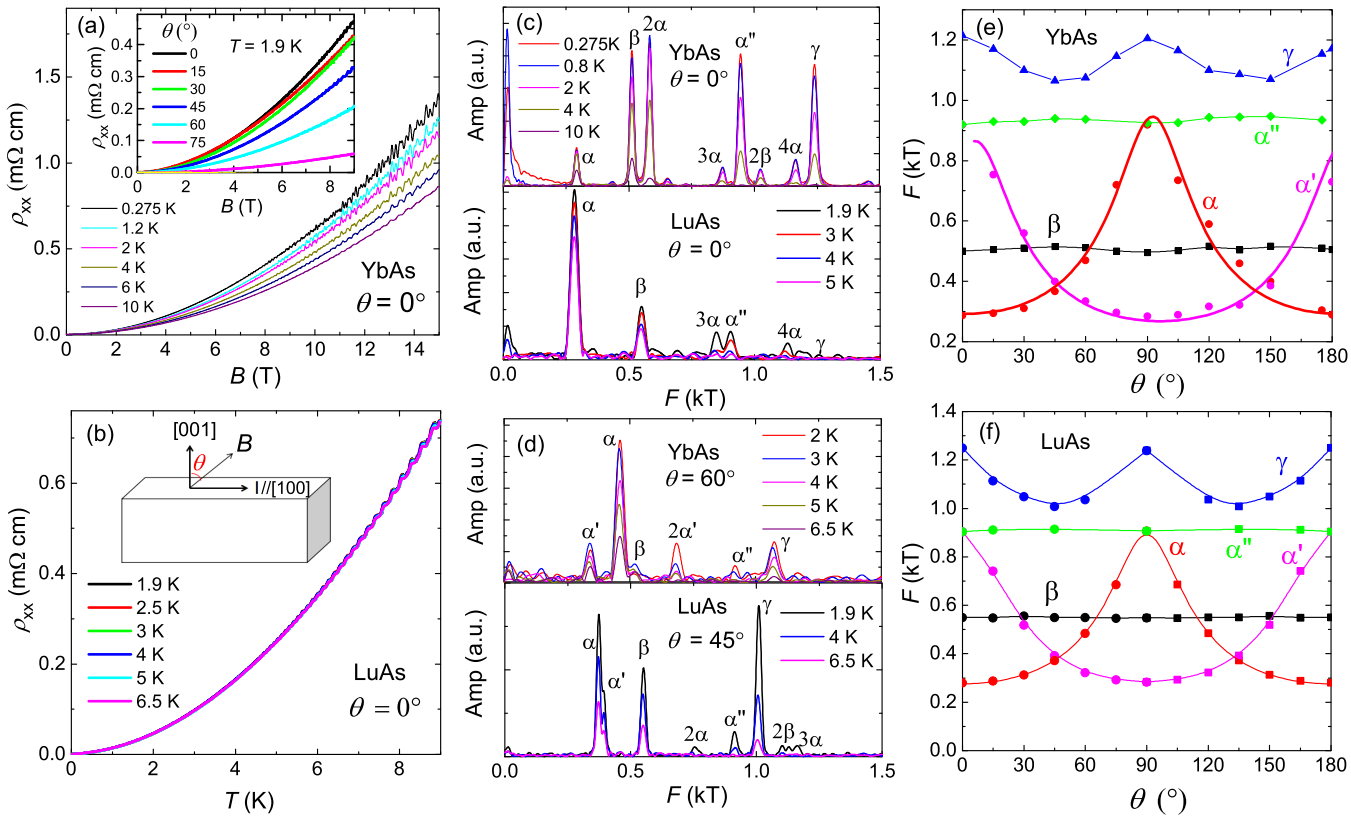

FIG. 6. Magnetic field dependence of the resistivity (ρ_{xx}) of (a) YbAs, and (b) LuAs. The inset of (a) shows the field dependence of ρ_{xx} of YbAs at different θ values at 1.9 K, where θ is the angle between the field direction and [001], as illustrated in the inset of (b). (c) Fast-Fourier-transform (FFT) analysis of the SdH oscillations at $\theta = 0^\circ$ for both YbAs (field range of 6–15 T) and LuAs (field range of 6–9 T), respectively. (d) FFT results at $\theta = 60^\circ$ for YbAs and $\theta = 45^\circ$ for LuAs, respectively, both in a field range of 6–9 T. (e) SdH oscillation frequencies as a function of θ for YbAs, obtained via an FFT analysis on the angle-dependent MR. The fitted curves described in the main text are shown by the thick lines for the α and α' bands, while the other thin lines are guides to the eyes. (f) SdH oscillation frequencies as a function of θ for LuAs. The thin solid lines are guides to the eyes. The frequencies F for $\theta > 90^\circ$ are mirrored from the 0°–90° data, in order to compare with YbAs.

10 K, indicating that the Fermi surface does not change with temperature in this range.

The respective angle dependencies of the SdH frequencies are displayed in Figs. 6(e) and 6(f), obtained from performing an FFT analysis on data at different angles in the field range of 6–9 T. The lines correspond to the five pockets, where the cross-sectional areas of the extremal orbits (A_{ext}) change upon rotating the field direction according to the Onsager relation $F \equiv (\Phi_0/2\pi^2)A_{\text{ext}}$, where Φ_0 is the magnetic flux quantum. The dispersions shown here are consistent with the dHvA results reported for YbAs in Ref. [39] and similar to those of LaAs [15]. In Ref. [39], four angle-dependent dispersion lines were observed for YbAs, three ellipsoidal electron pockets, and only one spherical hole pocket, which correspond to the α, α', α'' pockets and the β pocket in our data, respectively. The presence of at least one more hole pocket with a large effective mass was proposed based on the p-f mixing model [39]. Here we find that an extra hole pocket is indeed present (labeled as γ) for both YbAs and LuAs, which likely corresponds to a jack shape, as observed in LaAs [15,39]. The similar angle-dependent dispersions of YbAs to that of LuAs indicates that their Fermi surface geometries are nearly identical, implying that the Yb-4f electrons are well localized across the measured temperature range.

We calculated the carrier concentrations n of both electrons and holes, which are proportional to the volume V_{F} of the Fermi pockets via $n = V_{\text{F}}/4\pi^3$. Here the angular dependence of A_{ext} was used to extract the lengths of the semimajor and semiminor axes of the ellipsoidal pockets, as well as the radius of the spherical pocket. For the irregularly shaped γ pocket, V_F was estimated following the method used for LaAs in Ref. [15]. The calculated carrier densities are $n_e = 4.74 \times 10^{20}$ cm^{-3} and $n_e/n_h = 1.082$ for YbAs, and $n_e = 4.56 \times 10^{20}$ cm^{-3} with $n_e/n_h = 0.98$ for LuAs. The electron-hole compensation is consistent with the analysis of the MR and Hall resistivity, and moreover indicates that all the Fermi surface pockets in the Brillouin zone were detected from our SdH measurements.

For three-dimensional ellipsoidal pockets, the angular dependent quantum oscillation frequency $F(\theta)$ can be described by [57]

$$F(\theta) = A\pi ab/\sqrt{\sin^2(\theta+\varphi) + (a^2/b^2)\cos^2(\theta+\varphi)}, \quad (4)$$

where a and b are the lengths of the semimajor axis and semiminor axis of the ellipsoidal α pockets, respectively, A is a constant, and φ is an angular shift [57]. By using the above derived parameters a and b, it is shown in Fig. 6(e) that the

TABLE I. Comparison of effective carrier masses for the three bands obtained experimentally for YbAs and LuAs, together with the results from DFT calculation of YbAs. Besides those labeled with parentheses, the values are taken for $\theta = 0^\circ$.

	α (m_0)	β (m_0)	γ (m_0)
YbAs	0.175	0.256	0.541
LuAs	0.155	0.261	0.353(45°)
DFT	0.147	0.204	0.427, 0.350(45°)

angular dependence of the α and α' band frequencies of YbAs can be well accounted for by Eq. (4), with fitted values of $A = 3.35 \times 10^4$ Å^2 T and $\varphi = -1.26^\circ$.

The temperature dependence of the amplitudes for all the three bands at $\theta = 0^\circ$ were extracted, which were fitted using the Lifshitz-Kosevich (L-K) formula [58], as shown in Fig. 7(a). For the γ band, this yields an effective mass of 0.541 m_0 (m_0 is the free electron mass) and no anomaly is observed upon crossing T_N. However, for the α and β bands, which have lighter effective masses of 0.175 and 0.256 m_0, respectively, an abrupt increase of the amplitude is observed upon cooling below T_N. The effective mass of the α band is consistent with previously reported dHvA-effect measurements [39], where the increase in amplitude of the α band below T_N was explained as arising due to the combined effects of the spin factor and a change of Dingle temperature [39]. For LuAs, as shown in Fig. 7(b), the obtained effective masses for the α, β, and γ bands are 0.155, 0.261 and 0.353 m_0 (for $\theta = 45^\circ$), respectively. The results are summarized in Table I for comparison, where the effective masses obtained from DFT calculations for YbAs are also listed, assuming localized f electrons. This shows that similarly small effective charge carrier masses are deduced for YbAs and LuAs, which are well accounted for by the DFT calculations. The above analysis indicates that YbAs has a similar Fermi surface to LuAs in the studied temperature range from 10 down to 0.275 K. The carrier effective masses of YbAs are not significantly enhanced compared to those of LuAs, indicating that down to at least T_N the $4f$ electrons are well localized in YbAs, and the electronic correlations do not lead to a large renormalization of carrier masses.

To examine the possible influence of the transitions at T_N and T_M on the Fermi surface, we analyzed the FFT in several temperature and field ranges, corresponding to different phases in the B-T phase diagram shown in Fig. 2(b). The results displayed in Fig. 7(c) indicate that the SdH frequencies are nearly unchanged, suggesting that the Fermi surface volume is not modified upon crossing T_N or T_M.

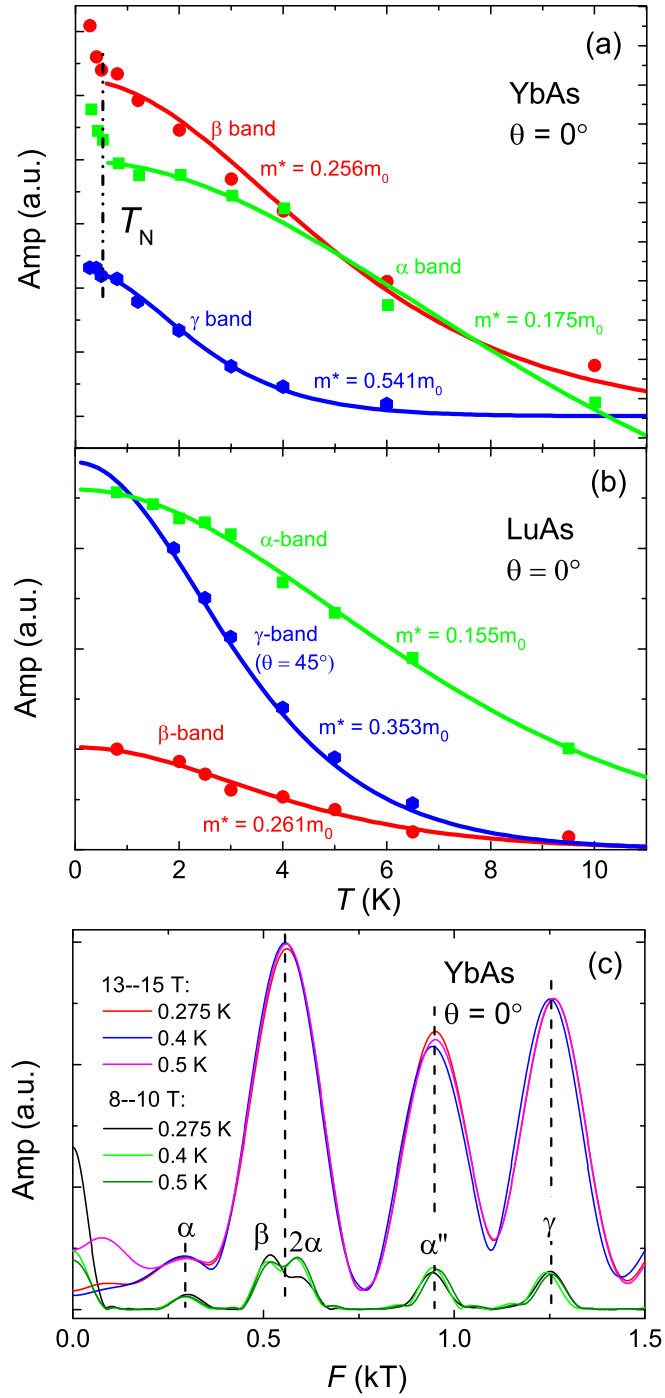

FIG. 7. Temperature dependence of the SdH oscillation amplitudes of all three bands for (a) YbAs (field range of 6–11 T) and (b) LuAs (field range of 6–9 T). The solid lines show the results of fitting with the L-K formula. The effective masses for the bands are labeled. (c) FFT analysis for YbAs at three temperatures, both above and below T_N or T_M, which show negligible differences in the oscillation frequencies.

2. *DFT calculations and ARPES measurements*

To further study the Fermi surfaces and topology of YbAs, we performed DFT calculations and ARPES measurements down to 10 K. In Figs. 8(a) and 8(c) we show the calculated band structure and Fermi surface of YbAs. Figure 8(b) displays the ARPES energy vs momentum cut along the k_x direction at $k_y = 0$ and $k_z \approx 0$, while Fig. 8(d) shows the Fermi surface map in the k_x-k_y plane at $k_z \approx 0$. The ARPES spectra were taken at 60 eV, which corresponds to the $k_z = 0$ condition. From comparing the calculated results with the measured data, it is clear that the Fermi surfaces consist of two concentric hole pockets at the Γ point and three symmetry-equivalent electron pockets at the X points, which

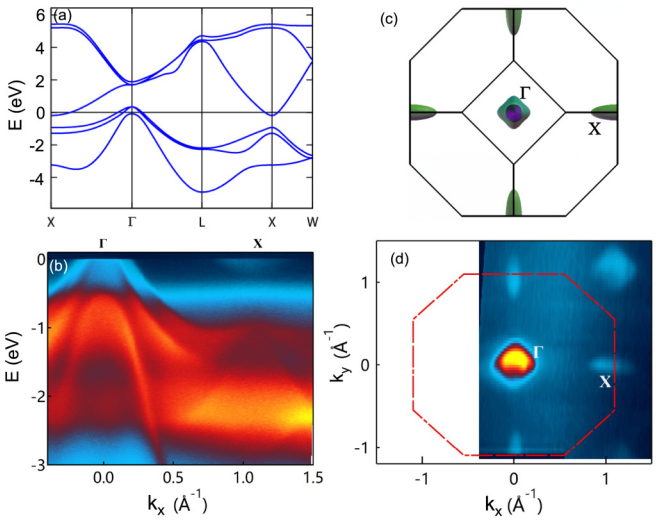

FIG. 8. (a) The calculated band structure of YbAs along high-symmetry lines. (b) ARPES energy-momentum cut along the k_x direction (Γ-X) at $k_y = 0$ and $k_z \approx 0$, to be compared with the Γ-X direction in (a). (c) The calculated 3D Fermi surfaces at $k_z = 0$ viewed from the z direction. (d) Experimental Fermi surface in the k_x-k_y plane near $k_z = 0$. The photon energy used for (b) and (d) is 60 eV, which corresponds to the $k_z = 0$ cut. The broken red line sketches the Brillouin zone (BZ).

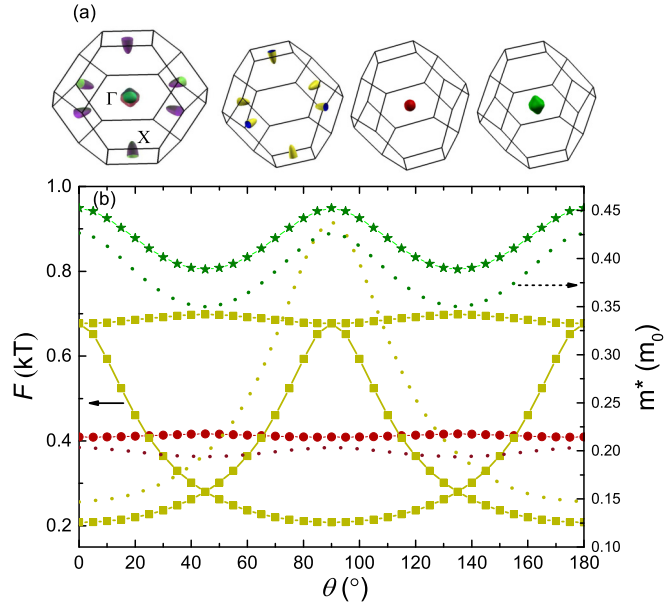

FIG. 9. (a) The calculated Fermi surfaces of YbAs, including electron pockets (dark yellow) at the X points and hole pockets (dark red and dark green) around the Γ point in the Brillouin zone. (b) The calculated angle-dependent dispersions of the FFT frequencies based on the Fermi pockets shown in (a) and the corresponding effective masses of the respective bands (shown by dotted lines).

are consistent with the results of our FFT analysis. In general, the ARPES spectra are in good agreement with the DFT calculations, indicating that the f electrons are mostly localized. In Figs. 8(a) and 8(b) no band inversion along the Γ-X direction can be observed, unlike the rare-earth monobismuthides [30], indicating the topologically trivial nature of YbAs, similar to LaAs [15]. This could be a consequence of the weaker spin-orbit coupling induced by As compared to Bi.

To highlight the different parts of the Fermi surface, we show the separated pockets in Fig. 9 together with the calculated angle-dependent dispersions of the FFT frequencies. These dispersions agree well with our FFT analysis displayed in Fig. 6(d), while the systematic differences in the values of the frequencies may arise from the presence of possible correlations in YbAs. Furthermore, the angle-dependent effective masses of the respective bands are also calculated, shown in Fig. 9(b) as dotted lines. This further indicates that the effective masses are small along all directions for all bands, with the values at $\theta = 0^\circ$ reasonably consistent with the experimental results.

Furthermore, Fig. 8(b) shows that no coherent bulk $4f$ band, i.e., the Kondo resonance peak, can be observed near the Fermi level, which indicates that the heavy fermion state has not developed down to 10 K. To confirm that the absence of a Kondo resonance peak is not due to a diminishing photoexcitation cross section, we employed a large range of photon energies (from 30 up to 200 eV) to search for any weak signature of a Kondo resonance peak near the Fermi level. Nevertheless, all our ARPES spectra show similar flat f bands at -1 and -2.1 eV [as shown in Fig. 8(b)], which are far away from the Fermi level and therefore are different from the bulk Kondo resonance that always resides near the Fermi level. A large-energy-range spectrum with its angle-integrated energy distribution curve is shown in Fig. 10, which reveals multiple intense Yb^{3+} peaks ranging from -12 to -6 eV, and weak Yb^{2+} peaks at -1 and -2.1 eV, respectively. The sharp Yb^{3+} peaks confirm that the valence of Yb is mainly trivalent in YbAs, while the weak peaks at -1 and -2.1 eV are most likely due to surface Yb^{2+} contributions, as seen in many Yb-based heavy fermion compounds [59]. Temperature dependent scans were also performed from 13 up to 80 K, but no signature of a Kondo resonance peak near the Fermi level can be observed and the band structure shows essentially no temperature dependence. This indicates that the many-body Kondo screening is rather weak at temperatures of 10 K and above.

IV. SUMMARY

In summary, we have grown high-quality single crystals of YbAs and performed a detailed study of the magnetotransport and ARPES measurements, together with DFT calculations. From low temperature resistivity measurements, we constructed a temperature-field phase diagram of YbAs for $B \perp [100]$, where we find a different field-induced first-order phase transition at high fields ($\geqslant$11 T). Moreover, XMR is observed in YbAs, and our analysis of the MR and Hall resistivity indicates that electron-hole compensation with enhanced carrier mobilities is the main mechanism leading to this behavior. However, upon comparing with the MR data of LuAs, distinct anomalies are discerned at low temperatures in YbAs, which are attributed to the short-range magnetic correlations revealed by INS measurements [46,47].

SdH oscillations for YbAs and LuAs reveal the presence of three electron and two hole pockets, where light effective

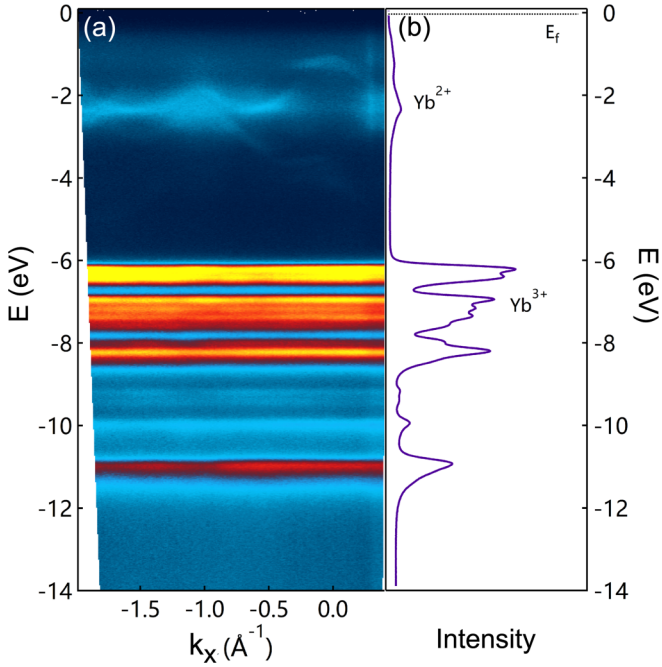

FIG. 10. (a) Large energy scale ARPES spectrum along the k_x direction at $k_y = 0$ taken with 90 eV photons and (b) the angle-integrated energy distribution curves showing the spin-orbit split Yb^{4+} $4f$ states at -1 and -2 eV, and multiple Yb^{3+} $4f$ states between -6 and -12 eV.

carrier masses are deduced from an analysis of the temperature dependence of the oscillation amplitudes down to 0.5 K. Together with ARPES measurements and DFT calculations, we found that the Fermi surface of YbAs is similar to that of nonmagnetic LuAs, indicating that the $4f$ electrons are well localized over the analyzed temperature range. Since the enhanced Sommerfeld coefficient and nuclear relaxation rate $1/(T_1T)$ were deduced from measurements below 0.3 K [37,45], it is possible that the system only displays heavy fermion behavior at temperatures lower than the present study. The magnetic ordering temperature of YbAs ($T_N = 0.5$ K) is much lower than the estimated energy scale of the magnetic exchange interactions (≈10 K) from Mössbauer spectroscopy [34], which was originally attributed to the presence of a significant Kondo effect [34,36,45]. However, we note that type-III AFM order on a face-centered-cubic lattice, as in the case of YbAs, can also exhibit strong magnetic frustration [60], which could be the origin of both the low T_N and the existence of short-range correlations at elevated temperatures.

Finally, ARPES and DFT calculations reveal a lack of band inversions in YbAs, indicating a topologically trivial electronic structure. While therefore YbAs does not exhibit the coexistence of magnetism and topological band structures, our results show that the XMR is significantly influenced by the presence of short-ranged magnetic correlations arising from localized electronic moments.

ACKNOWLEDGMENTS

We thank C. Y. Guo, T. Shang, and L. Jiao for their helpful suggestions. This work was supported by the National Key R&D Program of China (Grants No. 2017YFA0303100 and No. 2016YFA0300202), the National Natural Science Foundation of China (Grants No. U1632275, No. 11604291, and No. 11974306), and the Science Challenge Project of China (Project No. TZ2016004). This research used resources of the Advanced Light Source, which is a DOE Office of Science User Facility under contract No. DE-AC02-05CH11231. Y. Wu thanks Dr. P. Chen for the assistance in the ARPES experiments.

[1] M. Dzero, K. Sun, V. Galitski, and P. Coleman, Topological Kondo Insulators, Phys. Rev. Lett. **104**, 106408 (2010).

[2] S. Wolgast, Ç. Kurdak, K. Sun, J. W. Allen, D.-J. Kim, and Z. Fisk, Low-temperature surface conduction in the Kondo insulator SmB_6, Phys. Rev. B **88**, 180405(R) (2013).

[3] R. S. Mong, A. M. Essin, and J. E. Moore, Antiferromagnetic topological insulators, Phys. Rev. B **81**, 245209 (2010).

[4] J. Li, Y. Li, S. Du, Z. Wang, B.-L. Gu, S.-C. Zhang, K. He, W. Duan, and Y. Xu, Intrinsic magnetic topological insulators in van der Waals layered $MnBi_2Te_4$-family materials, Sci. Adv. **5**, eaaw5685 (2019).

[5] C. Liu, Y. Wang, H. Li, Y. Wu, Y. Li, J. Li, K. He, Y. Xu, J. Zhang, and Y. Wang, Robust axion insulator and Chern insulator phases in a two-dimensional antiferromagnetic topological insulator, Nat. Mater. (2020), doi:10.1038/s41563-019-0573-3.

[6] Y. Deng, Y. Yu, M. Z. Shi, Z. Guo, Z. Xu, J. Wang, X. H. Chen, and Y. B. Zhang, Quantum anomalous Hall effect in intrinsic magnetic topological insulator MnBi2Te4, Science eaax8156 (2020).

[7] Z. J. Wang, M. G. Vergniory, S. Kushwaha, M. Hirschberger, E. V. Chulkov, A. Ernst, N. P. Ong, R. J. Cava, and B. A. Bernevig, Time-Reversal-Breaking Weyl Fermions in Magnetic Heusler Alloys, Phys. Rev. Lett. **117**, 236401 (2016).

[8] Q. Xu, E. Liu, W. Shi, L. Muechler, J. Gayles, C. Felser, and Y. Sun, Topological surface Fermi arcs in the magnetic Weyl semimetal $Co_3Sn_2S_2$, Phys. Rev. B **97**, 235416 (2018).

[9] E. Liu, Y. Sun, N. Kumar, L. Muechler, A. Sun, L. Jiao, S.-Y. Yang, D. Liu, A. Liang, Q. Xu, J. Kroder, V. Suß, H. Borrmann, C. Shekhar, Z. S. Wang, C. Y. Xi, W. H. Wang, W. Schnelle, S. Wirth, Y. Chen, S. T. B. Goennenwein, and C. Felser, Giant anomalous Hall effect in a ferromagnetic kagome-lattice semimetal, Nat. Phys. **14**, 1125 (2018).

[10] Q. Wang, Y. Xu, R. Lou, Z. Liu, M. Li, Y. Huang, D. Shen, H. Weng, S. Wang, and H. Lei, Large intrinsic anomalous Hall effect in half-metallic ferromagnet $Co_3Sn_2S_2$ with magnetic Weyl fermions, Nat. Commun. **9**, 3681 (2018).

[11] H.-H. Lai, S. E. Grefe, S. Paschen, and Q. Si, Weyl-Kondo semimetal in heavy fermion systems, Proc. Natl. Acad. Sci. USA **115**, 93 (2018).

[12] C. Y. Guo, F. Wu, Z. Z. Wu, M. Smidman, C. Cao, A. Bostwick, C. Jozwiak, E. Rotenberg, Y. Liu, F. Steglich, and H. Q. Yuan, Evidence for Weyl fermions in a canonical heavy-fermion semimetal YbPtBi, Nat. Commun. **9**, 4622 (2018).

[13] D. X. Li, A. Oyamada, K. Hashi, Y. Haga, T. Matsumura, H. Shida, T. Suzuki, T. Kasuya, A. Dönni, and F. Hulliger, Study

of physical properties of Yb-monopnictides, J. Magn. Magn. Mater. **140**, 1169 (1995).

[14] C. Y. Guo, C. Cao, M. Smidman, F. Wu, Y. J. Zhang, F. Steglich, F.-C. Zhang, and H. Q. Yuan, Possible Weyl fermions in the magnetic Kondo system CeSb, npj Quantum Mater. **2**, 39 (2017).

[15] H.-Y. Yang, T. Nummy, H. Li, S. Jaszewski, M. Abramchuk, D. S. Dessau, and F. Tafti, Extreme magnetoresistance in the topologically trivial lanthanum monopnictide LaAs, Phys. Rev. B **96**, 235128 (2017).

[16] F. F. Tafti, Q. D. Gibson, S. K. Kushwaha, N. Haldolaarachchige, and R. J. Cava, Resistivity plateau and extreme magnetoresistance in LaSb, Nat. Phys. **12**, 272 (2015).

[17] L. K. Zeng, R. Lou, D.-S. Wu, Q. N. Xu, P. J. Guo, L.-Y. Kong, Y. G. Zhong, J. Z. Ma, B. B. Fu, P. Richard, P. Wang, G. T. Liu, L. Lu, Y. B. Huang, C. Fang, S. S. Sun, Q. Wang, L. Wang, Y. G. Shi, H. M. Weng, H.-C. Lei, K. Liu, S.-C. Wang, T. Qian, J. L. Luo, and H. Ding, Compensated Semimetal LaSb with Unsaturated Magnetoresistance, Phys. Rev. Lett. **117**, 127204 (2016).

[18] S. Sun, Q. Wang, P.-J. Guo, K. Liu, and H. Lei, Large magnetoresistance in LaBi: Origin of field-induced resistivity upturn and plateau in compensated semimetals, New J. Phys. **18**, 082002 (2016).

[19] N. Kumar, C. Shekhar, S. C. Wu, I. Leermakers, O. Young, U. Zeitler, B. Yan, and C. Felser, Observation of pseudo-two-dimensional electron transport in the rock salt-type topological semimetal LaBi, Phys. Rev. B **93**, 241106(R) (2016).

[20] J. Nayak, S.-C. Wu, N. Kumar, C. Shekhar, S. Singh, J. Fink, E. E. D. Rienks, G. H. Fecher, S. S. P. Parkin, B. Yan *et al.*, Multiple Dirac cones at the surface of the topological metal LaBi, Nat. Commun. **8**, 13942 (2017).

[21] O. Pavlosiuk, M. Kleinert, P. Swatek, D. Kaczorowski, and P. Wiśniewski, Fermi surface topology and magnetotransport in semimetallic LuSb, Sci. Rep. **7**, 12822 (2017).

[22] Y. Y. Wang, L. L. Sun, S. Xu, Y. Su, and T. L. Xia, Unusual magnetotransport in holmium monoantimonide, Phys. Rev. B **98**, 045137 (2018).

[23] H. Y. Yang, J. Gaudet, A. A. Aczel, D. E. Graf, P. Blaha, B. D. Gaulin, and F. Tafti, Interplay of magnetism and transport in HoBi, Phys. Rev. B **98**, 045136 (2018).

[24] T. J. Nummy, J. A. Waugh, S. P. Parham, Q. H. Liu, H.-Y. Yang, H. X. Li, X. Q. Zhou, N. C. Plumb, F. F. Tafti, and D. S. Dessau, Measurement of the atomic orbital composition of the near-Fermi-level electronic states in the lanthanum monopnictides LaBi, LaSb, and LaAs, npj Quantum Mater. **3**, 24 (2018).

[25] N. Wakeham, E. D. Bauer, M. Neupane, and F. Ronning, Large magnetoresistance in the antiferromagnetic semimetal NdSb, Phys. Rev. B **93**, 205152 (2016).

[26] M. Neupane, M. M. Hosen, I. Belopolski, N. Wakeham, K. Dimitri, N. Dhakal, J.-X. Zhu, M. Z. Hasan, E. D. Bauer, and F. Ronning, Observation of Dirac-like semi-metallic phase in NdSb, J. Phys.: Condens. Matter **28**, 23LT02 (2016).

[27] Y. Wang, Y. Wang, C. Y. Xi, L. S. Ling, S. L. Zhang, L. He, T. Han, H. Han, J. Yang, D. Liang, J. Gong, L. Luo, W. Tong, L. Zhang, Z. Qu, Y. Y. Han, W. K. Zhu, L. Pi, C. Zhang, and Y. Zhang, Observations of topological semimetal state and field-induced Fermi surface change in the antiferromagnetic monopnictide NdSb, Phys. Rev. B **97**, 115133 (2018).

[28] F. Wu, C. Y. Guo, M. Smidman, J. L. Zhang, and H. Q. Yuan, Large magnetoresistance and Fermi surface topology of PrSb, Phys. Rev. B **96**, 125122 (2017).

[29] F. Wu, C. Y. Guo, M. Smidman, J. L. Zhang, Y. Chen, J. Singleton, and H. Q. Yuan, Anomalous quantum oscillations and evidence for a non-trivial Berry phase in SmSb, npj Quantum Mater. **4**, 20 (2019).

[30] P. Li, Z. Z. Wu, F. Wu, C. Cao, C. Y. Guo, Y. Wu, Y. Liu, Z. Sun, C. M. Cheng, D. S. Lin, F. Steglich, H. Q. Yuan, T. C. Chiang, and Y. Liu, Tunable electronic structure and surface states in rare-earth monobismuthides with partially filled *f* shell, Phys. Rev. B **98**, 085103 (2018).

[31] Z. Z. Wu, F. Wu, P. Li, C. Y. Guo, Y. Liu, Z. Sun, C.-M. Cheng, T.-C. Chiang, C. Cao, H. Q. Yuan, and Y. Liu, Probing the origin of extreme magnetoresistance in Pr/Sm mono-antimonides/bismuthides, Phys. Rev. B **99**, 035158 (2019).

[32] X. Duan, F. Wu, J. Chen, P. Zhang, Y. Liu, H. Yuan, and C. Cao, Tunable electronic structure and topological properties of LnPn (Ln = Ce, Pr, Sm, Gd, Yb Pn = Sb, Bi), Commun. Phys. **1**, 71 (2018).

[33] H. R. Ott, H. Rudigier, and F. Hulliger, Low temperature phase transitions in Yb monopnictides, Solid State Commun. **55**, 113 (1985).

[34] P. Bonville, J. A. Hodges, F. Hulliger, P. Imbert, G. Jéhanno, J. B. Marimon da Cunha, and H. R. Ott, ^{170}Yb Mössbauer study of the heavy-electron pnictides YbP, YbAs and YbSb, J. Magn. Magn. Mater. **76–77**, 473 (1988).

[35] A. Dönni, P. Fischer, A. Furrer, and F. Hulliger, Long-range fcc antiferromagnetic ordering of type III in YbAs, Solid State Commun. **71**, 365 (1989).

[36] P. Bonville, J. A. Hodges, F. Hulliger, P. Imbert, G. Jéhanno, J. B. Marimon da Cunha, and H. R. Ott, First-order Kondo-frustrated antiferromagnetic ordering in the heavy electron compound YbAs, Hyperfine Interact. **40**, 381 (1988).

[37] K. Hashi, A. Oyamada, S. Maegawa, T. Goto, D. X. Li, and T. Suzuki, NMR study of a heavy Fermion compound YbAs, J. Phys. Soc. Jpn. **67**, 4260 (1998).

[38] A. Oyamada, C. Ayache, T. Suzuki, J. Rossat-Mignod, and T. Kasuya, Transport properties of YbAs and YbP, J. Magn. Magn. Mater. **90–91**, 443 (1990).

[39] N. Takeda, K. Tanaka, M. Kagawa *et al.*, de Haas-van Alphen Studies of YbAs above and below Néel Temperatur, J. Phys. Soc. Jpn. **62**, 2098 (1993).

[40] S. Takagi, A. Oyamada, and T. Kasuya, ^{31}P NMR studies of the magnetically ordered heavy-electron compound YbP, J. Phys. Soc. Jpn. **57**, 1456 (1988).

[41] T. Kasuya, Magnetic polaron in Yb monopnictides, J. Phys. Soc. Jpn. **63**, 843 (1994).

[42] T. Kasuya, Physics in low carrier strongly correlated systems: Kondo insulator magnetic polaron and high T_c, Physica B **215**, 88 (1995).

[43] T. Kasuya and D. X. Li, Charge dipolar ordering in Yb monopnictides, J. Phys. Soc. Jpn. **66**, 1587 (1994).

[44] P. Bonville, Kondo effect and heavy fermions in Yb compounds, Hyperfine Interact. **40**, 15 (1988).

[45] T. Sakon, N. Sato, A. Oyamada, N. Takeda, T. Suzuki, and T. Komatsubara, Heavy-electron behavior in a

low-carrier-concentration compound YbAs, J. Phys. Soc. Jpn. **61**, 2209 (1992).

[46] K. Ohoyama, M. Kohgi, K. Hashi, A. Oyamada, and T. Suzuki, A study of short-range spin correlations in Yb monopnictides, J. Magn. Magn. Mater. **177**, 339 (1998).

[47] K. Ohoyama, T. Osakabe, A. Dönni, M. Kohgi, A. Oyamada, and T. Suzuki, Anomalous short-range spin correlations in Yb monopnictides, Physica B **213**, 119 (1995).

[48] Y. Okayama, N. Môri, A. Oyamada, and T. Suzuki, Pressure effect on the magnetic ordering in YbAs, Physica B **259**, 148 (1999).

[49] O. Żogał, R. Wawryk, M. Matusiak, and Z. Henkie, Electron transport and magnetic properties of semimetallic LuAs, J. Alloys Compd. **587**, 190 (2014).

[50] L. Keller, P. Fischer, A. Furrer, A. Dönni, D. X. Li, and T. Suzuki, Giant quadrupolar interaction in the heavy fermion compound YbAs, Physica B **186-188**, 553 (1993).

[51] P. J. von Ranke, A. L. Lima, E. P. Nobrega, X. A. da Silva, A. P. Guimarães, and I. S. Oliveira, Anomalous magnetocaloric effect in YbAs associated with the giant quadrupolar interaction, Phys. Rev. B **63**, 024422 (2000).

[52] I. Ishii, T. Mizuno, K. Takezawa, S. Kumano, Y. Kawamoto, T. Suzuki, D. I. Gorbunov, M. S. Henriques, and A. V. Andreev, Magnetic-field-induced quadrupolar ordering and the crystal electric field effect in the distorted kagome lattice antiferromagnet $Dy_3Ru_4Al_{12}$, Phys. Rev. B **97**, 235130 (2018).

[53] S. Kamikawa, I. Ishii, K. Takezawa, T. Sakami, F. Nakagawa, H. Tanida, M. Sera, and T. Suzuki, Field induced phase transition with quadrupole fluctuation in $HoFe_2Al_{10}$ with orthorhombic symmetry, J. Phys. Soc. Jpn. **86**, 044601 (2017).

[54] Y. L. Wang, L. R. Thoutam, Z. L. Xiao, J. Hu, S. Das, Z. Q. Mao, J. Wei, R. Divan, A. Luican-Mayer, G. W. Crabtree, and W. K. Kwok, Origin of the turn-on temperature behavior in WTe_2, Phys. Rev. B **92**, 180402(R) (2015).

[55] J. M. Ziman, *Electrons and Phonons: The Theory of Transport Phenomena in Solids* (Oxford University Press, Oxford, UK, 2001).

[56] T. Suzuki, Fundamental physical properties of low carrier systems in Ce and Yb monopnictides, J. Alloys Compd. **192**, 231 (1993).

[57] J. M. Schneider, B. A. Piot, I. Sheikin, and D. K. Maude, Using the de Haas-van Alphen Effect to Map Out the Closed Three-Dimensional Fermi Surface of Natural Graphite, Phys. Rev. Lett. **108**, 117401 (2012).

[58] D. Shoenberg, *Magnetic Oscillations in Metals* (Cambridge University Press, Cambridge, UK, 2009).

[59] S. Fujimori, Band structures of 4*f* and 5*f* materials studied by angle-resolved photoelectron spectroscopy, J. Phys.: Condens. Matter **28**, 153002 (2016).

[60] T. Chatterji, L. P. Regnault, S. Ghosh and A. Singh, Magnetic excitations in frustrated fcc type-III antiferromagnet MnS_2, J. Phys.: Condens. Matter **31**, 125802 (2019).